Inorganic Chemistry
Article
Cite This: Inorg. Chem. 2019, 58, 7078−7090
pubs.acs.org/IC

Two Penta-RE^{III} Encapsulated Tetravacant Dawson Selenotungstates and Nanoscale Derivatives and Their Luminescence Properties

Yan Zhang, Yamin Li, Jingjing Pang, Yifan Liu, Pan Li, Lijuan Chen,* and Junwei Zhao*

Henan Key Laboratory of Polyoxometalate Chemistry, College of Chemistry and Chemical Engineering, Henan University, Kaifeng, Henan 475004, People's Republic of China

Supporting Information

ABSTRACT: Two penta-RE^{III} encapsulated tetravacant Dawson selenotungstates $[H_2N(CH_3)_2]_{10}H_3[SeO_4RE_5(H_2O)_7(Se_2W_{14}O_{52})_2]\cdot 40H_2O$ (RE = Dy^{3+} (**1**), Gd^{3+} (**2**)) were prepared by a one-step assembly strategy under bench conditions. Notably, the penta-RE^{III}-substituted $[SeO_4RE_5(H_2O)_7(Se_2W_{14}O_{52})_2]^{12-}$ polyoxoanion consists of two equivalent tetravacant Dawson $[Se_2W_{14}O_{52}]^{12-}$ fragments linked by a central penta-RE^{III} $\{SeO_4RE_5(H_2O)_7\}$ cluster through 16 lacunary oxygen atoms and four bridging oxygen atoms from two $[Se_2W_{14}O_{52}]^{12-}$ fragments. Furthermore, a series of cetyltrimethylammonium bromide (CTABr) encapsulated **1@CTA** nanomaterials were prepared by the microwave method by controlling different reaction times and temperatures. The effects of time and temperature on the morphologies of **1@CTA** nanomaterials were characterized by SEM images, and **1@CTA-5min** prepared at 80 °C has a relatively uniform size of about 190 nm. Moreover, the photoluminescence properties of **1** and **1@CTA** nanomaterials were investigated systematically, indicating that **1@CTA-5min** prepared at 80 °C exhibits the strongest emission due to its smallest size and high dispersion. The energy transfer from the ST fragments to Dy^{3+} ions in **1** and **1@CTA-5min** were proved by time-resolved emission spectra (TRES) and the change in CIE coordinates with increasing time, and their energy transfer mechanism diagram was demonstrated.

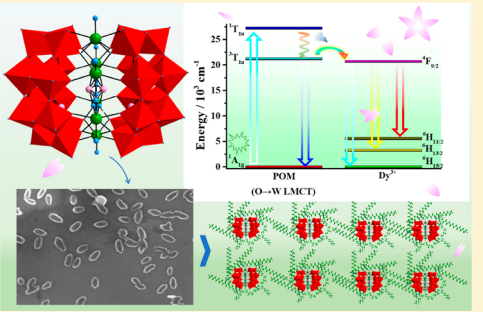

INTRODUCTION

Rare-earth (RE) oxide materials (REOMs) have attracted tremendous interest in various applications such as light-emitting diodes, optical amplifiers, lasers, etc. on account of their broad absorption from the ultraviolet to the near-infrared region, effective Stokes shifts, and multiple emission colors based on various optical energy levels.[1−3] Recently, numerous functionalized REOMs have been triumphantly manufactured by decomposition of RE hydroxides or nitrates at high temperatures.[4,5] Polyoxometalate (POM)-based materials can be formed by oxo-bridged early-transition-metal (TM) atoms in a d^0 or d^1 electronic configuration (usually Mo^{VI}, W^{IV}, V^V, Nb^V or Ta^V) and display changeable components, unique electronic structures, and reversible electrochemical properties, which make possible their wide use in diverse fields such as catalysis, magnetism, biology, and optics.[6−9] It is well-known that POM building blocks can serve as multifunctional inorganic polydentate O donors and provide extremely excellent binding opportunities for oxyphilic RE or TM ions to construct novel RE-substituted POM materials (RESPMs) or TM-substituted POM materials (TMSPMs) with intriguing structures and attractive properties.[10−17] It should be noted that the relative number of reports on RESPMs is much less than that on TMSPMs, probably because the larger ionic radius of RE ions cannot be sufficiently incorporated into the vacant sites of POM building blocks and the direct combination of highly oxyphilic RE ions with lacunary POM building blocks easily leads to amorphous precipitates.[18] Thus, the design and synthesis of novel RESPMs is still a particularly challenging and longstanding area of pursuit.

Since the first family of RE-substituted polytungstates $[REW_{10}O_{35}]^{7-}$ (RE = La^{3+}, Ce^{3+}, Pr^{3+}, Nd^{3+}, Sm^{3+}, Ho^{3+}, Er^{3+}, Yb^{3+}, Y^{3+}) was obtained by Peacock and Weakley in 1971,[19] various RESPMs have been successively discovered.[20−27] Obviously, the majority of the aforementioned RESPMs are RE-substituted arsenotungstates, because lacunary arsenotungstate precursors have been shown to be the most active building blocks to combine RE ions: in contrast, intensive investigations on RE-substituted selenotungstates (RESSTs) have lagged relatively behind due to the great difficulty in the preparation of selenotungstate (ST) precursors. Up to now, only several Keggin, Dawson, and Dawson-like RESSTs have been reported. For example, in 2013, Su's group succeeded in obtaining the two nanosized octameric RESSTs $[\{(SeO_3)W_{10}O_{34}\}_8\{Ce_8(H_2O)_{20}\}(WO_2)_4(W_4O_{12})]^{48-}$ (Figure 1a) and $[\{(SeO_3)_{10}O_{34}\}_8\{Ce_8(H_2O)_{20}\}(WO_2)_4\{(W_4O_6)Ce_4(H_2O)_{14}(SeO_3)_4(NO_3)_2\}]^{34-}$ (Figure 1b), in which cerium ions occupied the vacancy sites of Keggin $[SeW_9O_{33}]^{8-}$ segments and stabilized the whole structures.[28] Afterward, they reported two other cerium-substituted hexameric and tetrameric STs, $[Ce_6Se_6W_{67}O_{230}(OH)_6(H_2O)_{17}]^{22-}$ (Figure 1c) and $\{Ce(H_2O)_4[Ce_6Se_{10}W_{51}O_{187}(OH)_7(H_2O)_{18}]\}^{14-}$ (Figure 1d),

Received: March 14, 2019
Published: May 8, 2019

DOI: 10.1021/acs.inorgchem.9b00752
Inorg. Chem. 2019, 58, 7078−7090

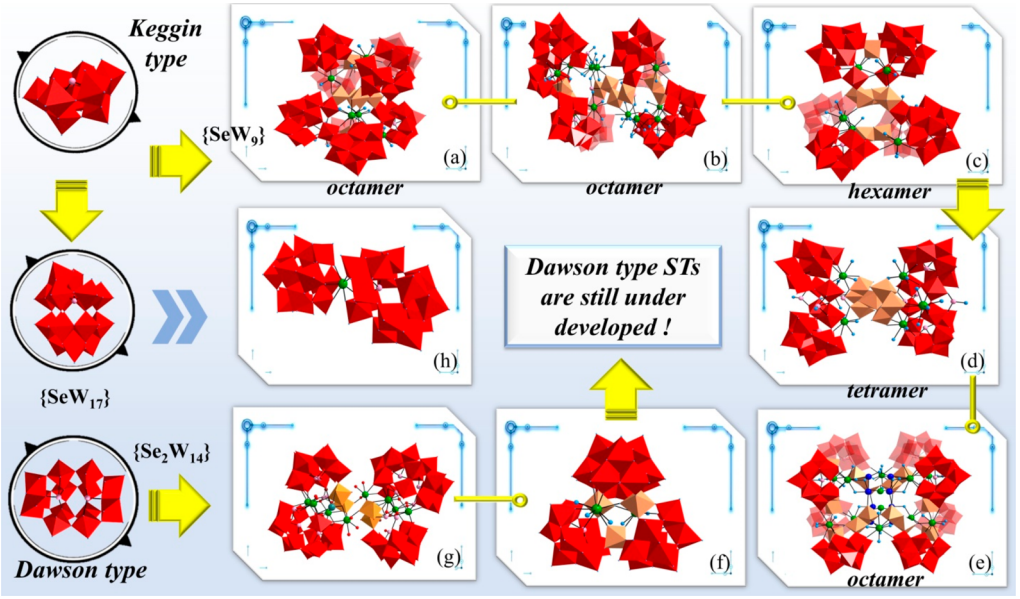

Figure 1. Summary of some reported RESSTs: (a) $[\{(SeO_3)W_{10}O_{34}\}_8\{Ce_8(H_2O)_{20}\}(WO_2)_4(W_4O_{12})]^{48-}$; (b) $[\{(SeO_3)W_{10}O_{34}\}_8\{Ce_8(H_2O)_{20}\}(WO_2)_4\{(W_4O_6)Ce_4(H_2O)_{14}(SeO_3)_4(NO_3)_2\}]^{34-}$; (c) $[Ce_6Se_6W_{67}O_{230}(OH)_6(H_2O)_{17}]^{22-}$; (d) $\{Ce(H_2O)_4[Ce_6Se_{10}W_{51}O_{187}(OH)_7(H_2O)_{18}]\}^{14-}$; (e) $\{[W_{18}RE_{10}(H_2O)_{34}O_{56}][B\text{-}\alpha\text{-}SeW_9O_{33}]_8\}^{38-}$; (f) $[(\alpha\text{-}SeW_9O_{33})_2\{Ce_2(H_2O)_4W_3O_6\}\{\alpha\text{-}Se_2W_{14}O_{51}(OH)\}]^{15-}$; (g) $[\{[RE_4W_4Se_4O_{22}(H_2O)_5](Se_2W_{14}O_{52})_2\}_2]^{32-}$; (h) $[Ce(SeW_{17}O_{59})_2]^{20-}$. Color scheme: $\{WO_6\}$ octahedra, red and wheat; Se, pink; RE, green; O, light blue.

which both comprise trivacant Keggin $[SeW_9O_{33}]^{8-}$ segments.[29] In 2017, our group discovered two types of organocounterion-assisted and pH-controlled high-nuclearity RESSTs, $\{[W_{18}RE_{10}(H_2O)_{34}O_{56}][B\text{-}\alpha\text{-}SeW_9O_{33}]_8\}^{38-}$ (Figure 1e) and $\{[W_{18}RE_{10}(H_2O)_{34}O_{56}][B\text{-}\alpha\text{-}SeW_9O_{33}]_8\}^{38-}$ (RE = La^{3+}, Ce^{3+}), constructed from eight trivacant Keggin $[B\text{-}\alpha\text{-}SeW_9O_{33}]^{8-}$ building blocks hinged by RE ions and additional W centers.[30] In 2014, the two mixed lacunary Keggin and Dawson RESSTs $[(\alpha\text{-}SeW_9O_{33})_2\{Ce_2(CH_3COO)(H_2O)_3W_3O_6\}(\alpha\text{-}Se_2W_{14}O_{52})]^{17-}$ and $[(\alpha\text{-}SeW_9O_{33})_2\{Ce_2(H_2O)_4W_3O_6\}\{\alpha\text{-}Se_2W_{14}O_{51}(OH)\}]^{15-}$ (Figure 1f) were discovered.[31] Recently, the family of RE and Se simultaneously bridging tetravacant Dawson STs $[\{[RE_4W_4Se_4O_{22}(H_2O)_5](Se_2W_{14}O_{52})_2\}_2]^{32-}$ (RE = Tb^{3+}, Dy^{3+}, Ho^{3+}, Er^{3+}, Tm^{3+}, Yb^{3+}) were successfully prepared by our group (Figure 1g).[32] In addition, the Dawson-like Ce-hybridizing ST $[Ce(SeW_{17}O_{59})_2]^{20-}$ was also reported in 2015 (Figure 1h).[33]

It is remarkable that most of the RESSTs reported above are cerium-substituted Keggin-type STs, which are constructed by trivacant $[SeW_9O_{33}]^{8-}$ units. To our knowledge, relevant explorations on other RESSTs and their luminescence properties are very underdeveloped to date. Moreover, the search for and discovery of Dawson-type RESSTs still remains an extreme challenge due to their potential appeal in constructing unparalleled structures and exploiting intriguing properties. With this background, as a part of our continuing work,[30,32,33] in this article we introduce Dy^{3+} and Gd^{3+} ions into the Se−W−RE system in order to prepare novel Dawson-type RESSTs by means of a one-pot in situ assembly reaction of $Na_2WO_4{\cdot}2H_2O$, $Dy(NO_3)_3{\cdot}6H_2O$, $Gd(NO_3)_3{\cdot}6H_2O$, and Na_2SeO_3 under weakly acidic aqueous conditions in the presence of dimethylamine hydrochloride. Through our experimental explorations and documented research,[32−35] we have found that pH has an essential role in constructing Dawson-type STs. When the final pH was kept at 4.0−6.0, the formation of Dawson-type STs is favored. Meanwhile, SeO_3^{2-} has a lone pair of electrons and has extreme ease in acting as an anionic template to construct multivacant ST segments during the course of preparing RESSTs. In addition, the resulting RESST polyanions can be easily be stabilized by the larger organoamine $[H_2N(CH_3)_2]^+$ countercations.[33,36] Thus, the two novel penta-RE^{III}-substituted tetravacant Dawson STs $[H_2N(CH_3)_2]_{10}H_3[SeO_4Dy_5(H_2O)_7(Se_2W_{14}O_{52})_2]{\cdot}40H_2O$ (**1**) and $[H_2N(CH_3)_2]_{10}H_3[SeO_4Gd_5(H_2O)_7(Se_2W_{14}O_{52})_2]{\cdot}40H_2O$ (**2**) were prepared and characterized by IR spectra, elemental analyses, and single-crystal X-ray diffraction.

On the other hand, nanosized REOMs exhibit unrivaled potential applications such as tunable chemical and physical properties and have aroused fascinating attention. Although some POM-based REOMs have been synthesized by solid-state chemical reactions,[37] microemulsion methods,[38] phase transfer,[39] ultrasonication,[40] etc., no nanosized RESST materials have been isolated through a microwave method. Cetyltrimethylammonium bromide (CTABr) can serve as a cationic surfactant to make soluble RE-substituted POM species precipitate and form various nanoscale CTA-functionalized RESPMs, which endows them with outstanding adjustable fluorescence properties.[41−43] Thus, in this article, we first utilized the microwave method to prepare a series of nanosized CTA-encapsulated RESST materials derived from **1** through changes in the reaction time and temperature. IR spectra exhibited that the skeleton of **1** did not collapse after **1** was functionalized by CTA^+ groups. As can be seen from the SEM images, the nanoscale particles have a uniform morphology with a size of about 190 nm when the reaction temperature and time are controlled at 80 °C and 5 min. Subsequent fluorescence experiments have proved that **1@CTA-5min** prepared at 80 °C has the highest emission intensity due to its smallest size and high dispersion. The energy transfer from the ST fragments to Dy^{3+} ions in **1** and **1@CTA-5min** were investigated by TRES, and the change in CIE coordinates with longer time and their energy transfer mechanism diagram are demonstrated and discussed. Moreover, the corresponding CIE

DOI: 10.1021/acs.inorgchem.9b00752
Inorg. Chem. 2019, 58, 7078−7090

Table 1. Crystallographic Data and Structure Refinements for 1 and 2

	1	2
empirical formula	$C_{20}H_{177}N_{10}Dy_5O_{155}Se_5W_{28}$	$C_{20}H_{177}N_{10}Gd_5O_{155}Se_5W_{28}$
formula wt	9393.82	9367.57
cryst syst	monoclinic	monoclinic
space group	$C2/m$	$C2/m$
a, Å	23.6590(14)	23.830(3)
b, Å	26.2335(17)	26.048(3)
c, Å	18.0329(11)	18.088(2)
α, deg	90	90
β, deg	126.3880(10)	126.0350(10)
γ, deg	90	90
V, Å^{-3}	9010.0(10)	9079.1(18)
Z	2	2
μ, mm^{-1}	20.953	20.562
F(000)	8358	8338.0
T, K	296(2)	296(2)
limiting indices	$-27 \le h \le 28$	$-18 \le h \le 28$
	$-31 \le k \le 27$	$-30 \le k \le 27$
	$-20 \le l \le 21$	$-21 \le l \le 19$
no. of rflns collected	23236	23118
no. of indep rflns	8057	8046
R_{int}	0.0625	0.0820
no. of data/restraints/params	8057/17/410	8046/59/403
GOF on F^2	1.034	0.986
final R indices ($I > 2\sigma(I)$)	R1 = 0.0510	R1 = 0.0583
	wR2 = 0.1207	wR2 = 0.1481
R indices (all data)	R1 = 0.0928	R1 = 0.0830
	wR2 = 0.1336	wR2 = 0.1619

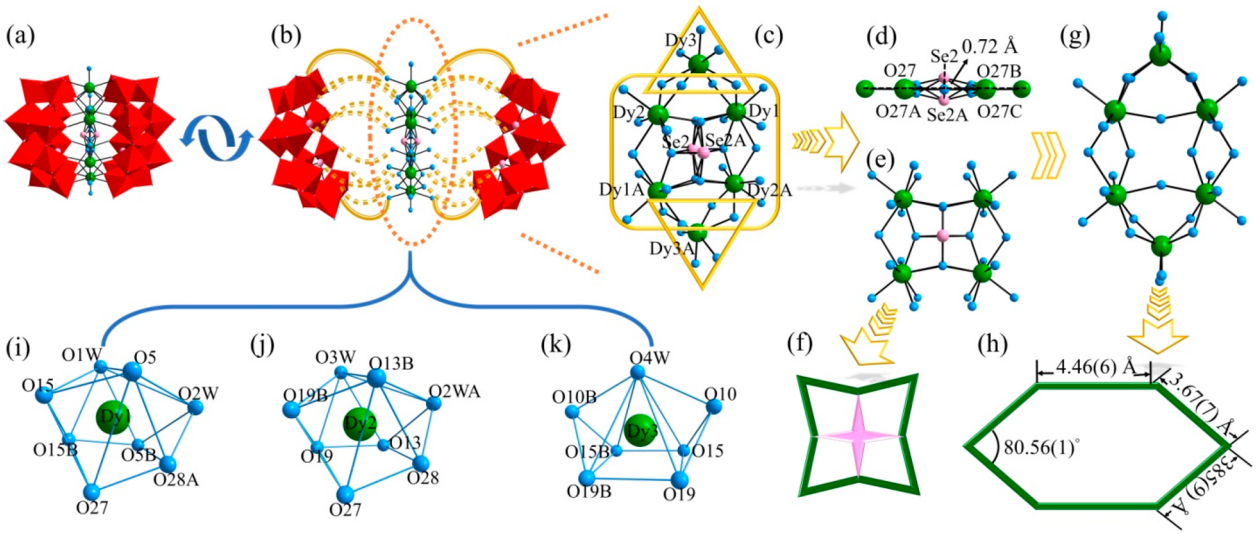

Figure 2. (a) Penta-Dy^{3+}-substituted polyoxoanion $[SeO_4Dy_5(H_2O)_7(Se_2W_{14}O_{52})_2]^{12-}$of **1**. (b) Connection mode between the $\{SeO_4Dy_5(H_2O)_7\}$ cluster and two tetravacant Dawson $[Se_2W_{14}O_{52}]^{12-}$ fragments in **1**. (c) View of the central penta-Dy^{3+} $\{SeO_4Dy_5(H_2O)_7\}$ cluster. (d) Se2 atom disordered over both sides of the square plane made up by $Dy1^{3+}$, $Dy2^{3+}$, $Dy1A^{3+}$, and $Dy2B^{3+}$ cations. (e) View of the square tetra-Dy^{3+} $\{SeO_4Dy_4(H_2O)_6\}$ cluster. (f) Simplified view of the square tetra-Dy^{3+} $\{SeO_4Dy_4(H_2O)_6\}$ cluster. (g) View of the penta-Dy^{3+} $\{Dy_5(H_2O)_7\}$ cluster. (h) Simplified view of the penta-Dy^{3+} $\{Dy_5(H_2O)_7\}$ cluster. (i) Bicapped-trigonal-prismatic geometry of the $Dy1^{3+}$ ion in **1**. (j) Bicapped-trigonal-prismatic geometry of the $Dy2^{3+}$ ion in **1**. (k) Bicapped-square-pyramidal geometry of the $Dy3^{3+}$ ion in **1**. Color scheme: WO_6 octahedra, red; Se, pink; Dy, green; O, light blue. The atoms with the suffixes A, B, and C are generated by symmetry operations where A denotes $1 - x, y, -z$ and B denotes $x, -y, z$.

coordinates and color purity parameters can be changed by different excitation wavelengths as well, which provides possibilities in developing and pursuing promising POM-based optical applications. This work gives useful guidance for the further development of novel luminescent RESPMs and the surfactant-encapsulated nanosized luminescent RESPMs.

RESULTS AND DISCUSSION

Structural Description. **1** and **2** were synthesized by the facile one-pot reaction of $Na_2WO_4{\cdot}2H_2O$, Na_2SeO_3, dimethylamine hydrochloride, $RE(NO_3){\cdot}6H_2O$,and 2,6-pyridinedicarboxylic acid. However no 2,6-pyridinedicarboxylic acid ligand is found in the structures of **1** and **2**. Experimental results showed

DOI: 10.1021/acs.inorgchem.9b00752
Inorg. Chem. 2019, 58, 7078−7090

that, when 2,6-pyridinedicarboxylic acid was removed from the reaction system, we could not obtain high yields of crystals of **1** and **2**, only low yields of crystals of **1** and **2** with amorphous precipitates, which indicates that 2,6-pyridinedicarboxylic acid has some synergistic effect together with other reactants in the formation of **1** and **2**. The measured PXRD patterns of **1** and **2** are quite consistent with the simulated XRD pattern from a single-crystal X-ray diffraction structural analysis (Figure S1). **1** and **2** are isomorphic and crystallize in the monoclinic space group *C*2/*m*. Crystallographic data and structural refinement parameters for **1** and **2** are demonstrated in Table 1. Only the structure of **1** is discussed here. The penta-Dy^{III}-substituted $[SeO_4Dy_5(H_2O)_7(Se_2W_{14}O_{52})_2]^{12-}$ polyoxoanion of **1** consists of two equivalent tetravacant Dawson $[Se_2W_{14}O_{52}]^{12-}$ fragments linked by a central penta-Dy^{3+} $\{SeO_4Dy_5(H_2O)_7\}$ cluster through 16 lacunary oxygen atoms and 4 bridging oxygen atoms from two $[Se_2W_{14}O_{52}]^{12-}$ fragments (Figure 2a,b). In the central penta-Dy^{3+} $\{SeO_4Dy_5(H_2O)_7\}$ cluster (Figure 2c), there are three cyrstallographically independent Dy^{3+} cations, namely, $Dy1^{3+}$, $Dy2^{3+}$, and $Dy3^{3+}$. It should be pointed out that the $Dy1^{3+}$ and $Dy2^{3+}$ cations are fully occupied with a site occupancy of 100% whereas the $Dy3^{3+}$ cation is half-occupied with a site occupancy of 50%. Alternatively, the $Dy3^{3+}$ cation is disordered over two positions (Dy3 and Dy3A) with a site occupancy of 50% for each position. A similar disorder phenomenon has been previously encountered.[44] In addition, the Se2 atom is also disordered over two positions (Se2 and Se2A) with a site occupancy of 50% for each position and O27 is disordered over two positions (O27 and O27A) with a site occupancy of 50% for each position. Upon an elaborative observation on the central penta-Dy^{3+} $\{SeO_4Dy_5(H_2O)_7\}$ cluster, the Se2 atom is disordered over both sides of the square plane made up by $Dy1^{3+}$, $Dy2^{3+}$, $Dy1A^{3+}$, and $Dy2A^{3+}$ cations and the distance between the Se2 atom and the square plane is 0.726(6) Å (Figure 2d). The disordered Se2 atom may play a vital role in stabilizing the centrosymmetric $\{SeO_4Dy_5(H_2O)_7\}$ cluster. Most interestingly, $Dy1^{3+}$, $Dy2^{3+}$, $Dy1A^{3+}$, and $Dy2A^{3+}$ cations in the central penta-Dy^{3+} $\{SeO_4Dy_5(H_2O)_7\}$ cluster are bridged together through a four-coordinate $\{SeO_4\}$ group (Figure 2e,f). The disordered $Dy3^{3+}$ cation caps both sides of the square tetra-Dy^{3+} $\{SeO_4Dy_4(H_2O)_6\}$ cluster (Figure 2c). To the best of our knowledge, this four-coordinate $\{SeO_4\}$ bridging group has been observed in POM chemistry for the first time. Of particular concern is that the skeleton of the penta-Dy^{3+} $\{Dy_5(H_2O)_7\}$ cluster is still retained (Figure 2g) when the four-coordinate $\{SeO_4\}$ bridging group is removed from the central penta-Dy^{3+} $\{SeO_4Dy_5(H_2O)_7\}$ cluster. In the penta-Dy^{3+} $\{Dy_5(H_2O)_7\}$ cluster, the Dy···Dy distances range from 3.67(7) to 4.46(6) Å and the Dy1−Dy3−Dy2 angle is 80.56(1)° (Figure 2h). It is interesting to note that all of the Dy^{3+} cations with different coordination geometries are linked to each other through an edge-sharing mode. Notably, the $Dy1^{3+}$ cation resides in an eight-coordinate bicapped-trigonal-prismatic geometry established by two μ_2-O atoms (O5, O5B) and two μ_3-O atoms (O15, O15B) from lacunary $[Se_2W_{14}O_{52}]^{12-}$ fragments (Dy−O: 2.30(6)−2.31(9) Å) and two coordinated water O atoms (O1W, O2W) (Dy−O: 2.37(3)−2.68(4) Å) (Figure 2i). Similarly, the eight-coordinate bicapped-trigonal-prismatic $Dy2^{3+}$ ion bonds to two μ_2-O atoms (O13, O13B) and two μ_3-O atoms (O19, O19B) from vacant sites of $[Se_2W_{14}O_{52}]^{12-}$ fragments (Dy−O: 2.29(8)−2.31(7) Å), two coordinated water O atoms (O3W, O2WA) (Dy−O: 2.33(2)−2.65(5) Å,) and O27, O28 atoms from a $\{SeO_4Dy_5(H_2O)_7\}$ cluster (Dy−O: 2.43(2)−2.49(3) Å) (Figure 2j). The $Dy3^{3+}$ cation has a bicapped-tetragonal-pyramidal geometry, in which the apical site of the square pyramid is occupied by the coordinated water atom O4W (Dy−O: 2.14(5) Å), four basal positions are taken by four lacunary O atoms (O15, O15B, O19, and O19B) from two $[Se_2W_{14}O_{52}]^{12-}$ fragments (Dy−O: 2.40(0)−2.43(8) Å), and two capped sites are taken by two bridging oxygen atoms (O10, O10B) from two $[Se_2W_{14}O_{52}]^{12-}$ fragments (Dy−O: 2.54(4) Å) (Figure 2k). Therein, $Dy1^{3+}$ and $Dy2^{3+}$ ions are bridged by disordered O27 atoms, $Dy1^{3+}$ and $Dy2A^{3+}$ ions are linked together by O28A and O27 atoms, and $Dy3^{3+}$, $Dy1^{3+}$ and $Dy3^{3+}$, $Dy2^{3+}$ ions have several bridges by disordered O15 atoms and O19 atoms. In addition, seven aqueous ligands associated with the $\{SeO_4Dy_5(H_2O)_7\}$ cluster increase the possibility of substitution by organic carboxylic ligands to give organic−inorganic hybrid RESSTs.

The sandwich-type $[SeO_4Dy_5(H_2O)_7(Se_2W_{14}O_{52})_2]^{12-}$ unit in **1** (Figure 3a) somewhat resembles the Fe^{III}-substituted

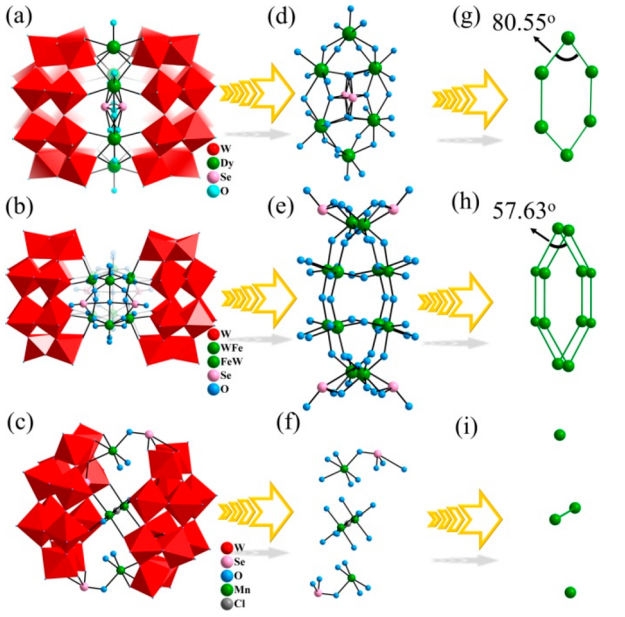

Figure 3. (a) View of the $[SeO_4Dy_5(H_2O)_7(Se_2W_{14}O_{52})_2]^{12-}$ unit in **1**. (b) View of the $[Fe_6Se_6W_{34}O_{124}(OH)_{16}]^{18-}$ unit. (c) View of the $[Mn_4Se_6W_{24}O_{94}Cl(H_2O)_6]^{13-}$ unit. (d) View of the central penta-Dy^{III} $\{SeO_4Dy_5(H_2O)_7\}$ cluster in **1**. (e) View of the heterometal Fe/W $\{Fe_6Se_2W_6\}$ cluster in $[Fe_6Se_6W_{34}O_{124}(OH)_{16}]^{18-}$. (f) View of the Se and Mn bridging atoms in $[(Se_2W_{12}O_{46})_2\{Mn_2Cl(H_2O)_2\}\{Mn(H_2O)_2\}_2(SeO)_2]^{13-}$. (g) Simplified view of the hexagon formed by the Dy^{3+} ions in the $\{SeO_4Dy_5(H_2O)_7\}$ cluster. (h) Simplified view of two hexagons formed by heterometal Fe/W centers in the $\{Fe_6Se_2W_6\}$ cluster. (i) Simplified view of the Se and Mn bridging atoms.

$[Fe_6Se_6W_{34}O_{124}(OH)_{16}]^{18-}$ (Figure 3b) and the Mn−Se−O bridging dimeric $[Mn_4Se_6W_{24}O_{94}Cl(H_2O)_6]^{13-}$ (Figure 3c).[34−45] Evidently, they are all derived from lacunary Dawson-type STs, in which the vacancies in the ST units are occupied by additional metal ions. Nevertheless, remarkable structural differences among them are perceived. (a) The building blocks in **1** and $[Fe_6Se_6W_{34}O_{124}(OH)_{16}]^{18-}$ are tetravacant Dawson-type $[Se_2W_{14}O_{52}]^{12-}$ fragments, while the building blocks in $[Mn_4Se_6W_{24}O_{94}Cl(H_2O)_6]^{13-}$ are hexavacant Dawson-type ST fragments. (b) The metal cations in the central cores linking two vacant Dawson-type ST fragments are different: the metal cations in **1** are RE ions, while the metal cations in $[Fe_6Se_6W_{34}O_{124}(OH)_{16}]^{18-}$ and $[Mn_4Se_6W_{24}O_{94}Cl(H_2O)_6]^{13-}$

DOI: 10.1021/acs.inorgchem.9b00752
Inorg. Chem. 2019, 58, 7078−7090

are TM cations. (c) The obvious differences in the central cores are that **1** contains a penta-Dy^{3+} $\{SeO_4Dy_5(H_2O)_7\}$ cluster (Figure 3d) and $[Fe_6Se_6W_{34}O_{124}(OH)_{16}]^{18-}$ includes a heterometallic Fe/W$\{Fe_6Se_2W_6\}$ cluster (Figure 3e), but the $[Mn_4Se_6W_{24}O_{94}Cl(H_2O)_6]^{13-}$ unit is formed by the Se and Mn atoms bridging two $[Se_2W_{12}O_{46}]^{12-}$ fragments (Figure 3f). (d) The Dy^{3+} ions in the penta-Dy^{3+} $\{SeO_4Dy_5(H_2O)_7\}$ cluster can be simplified to a hexagon (Figure 3g), and the heterometallic Fe/W centers in the $\{Fe_6Se_2W_6\}$ core can be seen as two hexagons (Figure 3h). In addition, the angle (80.55(1)°) of Dy1−Dy3−Dy2 in the simplified hexagon is larger than the angle (57.6(3)°) of Fe1/W9−Fe3/W11−Fe2/W10. Although reports on TM- or RE-substituted STs are burgeoning, those on sandwich-type STs are very limited; only $[Fe_6Se_6W_{34}O_{124}(OH)_{16}]^{18-}$ (Figure 3b) and $[Mn_4Se_6W_{24}O_{94}Cl(H_2O)_6]^{13-}$ (Figure 3c) have been isolated so far. As far as we know, a sandwich-type ST containing five Dy^{3+} ions has not been reported.

Furthermore, the space packing of **1** is quite interesting. In layer A or layer B, discrete $[SeO_4Dy_5(H_2O)_7(Se_2W_{14}O_{52})_2]^{12-}$ polyoxoanions of **1** are tidily distributed in an −AAA− fashion along the *b* or *c* axes (Figure S2a,b). However, in a view along the *a* axis, the two closed layers in the crystal lattice of **1** exhibit two types of stacking patterns to give rise to an organized −ABAB− pattern (Figure S2c,i), which contributes to reducing the steric hindrance as much as possible and enhancing the chemical stability of **1**.[45,46] Simultaneously, in order to clearly represent the packing arrangement along with the *a* axis, the simplified alignment of **1** is shown in Figure S2d−f. Upon further inspection, $[H_2N(CH_3)_2]^+$ countercations and solvent water molecules are filled in the gaps of the discrete polyoxoanions and interact with each other via electrostatic forces and hydrogen-bonding interactions with N−H···O distances of 2.96(2)−3.25(2) Å (Figure S2g,h).

Characterization of 1@CTA Nanomaterials. In order to intuitively observe the nanostructural details of **1@CTA-5min** prepared at 80 °C, the morphology of **1@CTA-5min** was studied by SEM images. As shown in Figure 4a−c, the spindle-shaped nanoparticles of **1@CTA-5min** are found to be comparatively uniform. Plotted size statistics of the spindle-shaped nanoparticles of **1@CTA-5min** are shown in Figure 4d; the normal distribution is in the range of 150−240 nm with an average of ca. 190 nm. According to EDS mapping images of **1@CTA-5min** (Figure 4e), the spatial distributions of C, W, and O elements in **1@CTA-5min** are uniform, indicating the successful composition of **1** and CTA. Furthermore, the hyperfine structure of **1@CTA-5min** possesses a distinct lattice fringe spacing of 3.46 nm in the HRTEM image (Figure 5a,b), which is near the distance between two polyoxoanion layers in the nano **1@CTA-5min** (Figure 5c,d). The result is consistent with the small-angle powder X-ray diffraction analysis that the characteristic peak at 2.47° corresponding to d = 3.57 nm according to the Bragg formula $2d \sin\theta = n\lambda$, where θ is the diffraction angle, λ is the wavelength of the X-ray beam with Cu Kα radiation (λ = 1.54056 Å) at 293 K, and n = 1 (Figure 5 and Figure S3).[47]

Because of strong electrostatic interactions between CTA cations and $[SeO_4Dy_5(H_2O)_7(Se_2W_{14}O_{52})_2]^{12-}$ polyoxoanions, the $[SeO_4Dy_5(H_2O)_7(Se_2W_{14}O_{52})_2]^{12-}$ polyoxoanions in **1@CTA-5min** are rearranged in comparison with the structure of **1**. The average diameter of a $[SeO_4Dy_5(H_2O)_7(Se_2W_{14}O_{52})_2]^{12-}$ polyoxoanion is about 1.50 nm according to the single-crystal X-ray diffraction analysis, and the length of the alkyl chain in a CTA cation with a planar zigzag conformation is estimated to be 2.18 nm, as is known from previously published reports.[48−50] Thus, the distance of two neighboring $[SeO_4Dy_5(H_2O)_7(Se_2W_{14}O_{52})_2]^{12-}$ polyoxoanion layers is calculated as 3.68 nm

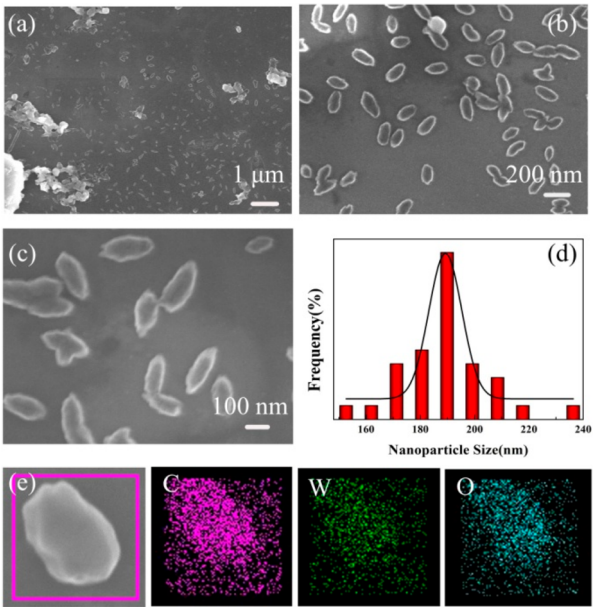

Figure 4. (a) SEM image of **1@CTA-5 min** (scale bar 1 μm). (b) SEM image of **1@CTA-5min** (scale bar 200 nm). (c) SEM image of **1@CTA-5min** (scale bar 100 nm). (d) Nanoparticle size distribution of **1@CTA-5min**. (e) EDS mapping images of **1@CTA-5min**.

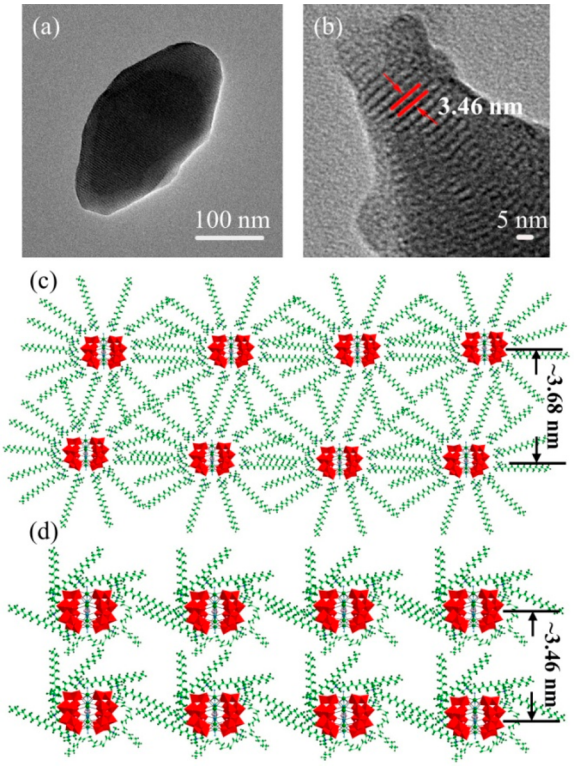

Figure 5. (a) TEM image of **1@CTA-5min** (scale bar 100 nm). (b) HRTEM image of **1@CTA-5min** (scale bar 5 nm). (c) Schematic illustration considering that the CTA chains are perpendicular to polyoxoanions. (d) Schematic illustration considering that the CTA chains surround polyoxoanions in the leaning mode. Color scheme: CTA, green; $[SeO_4Dy_5(H_2O)_7(Se_2W_{14}O_{52})_2]^{12-}$ polyoxoanions, red.

DOI: 10.1021/acs.inorgchem.9b00752
Inorg. Chem. 2019, 58, 7078−7090

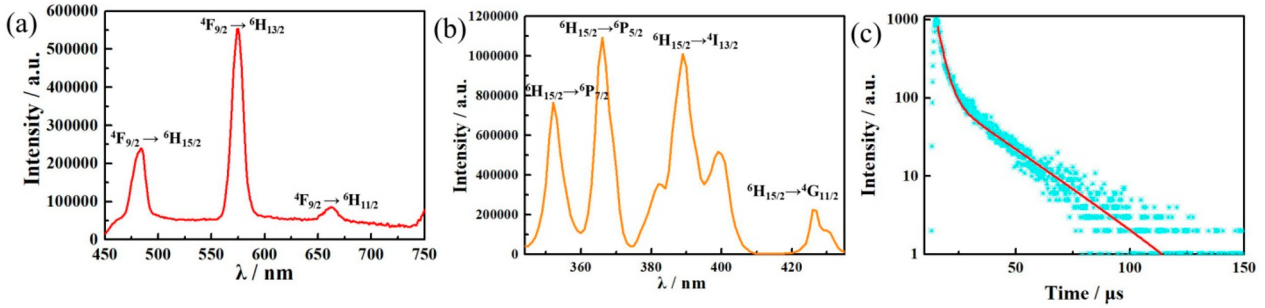

Figure 6. (a) Solid-state emission spectrum of **1** (λ_{ex} = 388 nm). (b) Solid-state excitation spectrum of **1** (λ_{em} = 574 nm). (c) Lifetime decay curve of **1** collected by monitoring the strongest emission of 574 nm.

(2.18 + 1.50 = 3.68 nm) ,considering that the CTA chains are perpendicular to polyoxoanions (Figure 5c). Obviously, the calculated value is larger than the experimental result (3.46 nm). Therefore, the CTA chains can surround polyoxoanions in the leaning mode.[51] The possible packing model is shown in Figure 5d.

To investigate the influence of assembly conditions on the size and morphology, we collected the intermediate morphologies at different times and heating temperature intervals. The morphology of the **1@CTA-3min** obtained is faveolate when the reaction time is 3min at 80 °C (Figure S4a). When the reaction time is increased to 5 min, comparatively uniform spindle-shaped nanoparticles of **1@CTA-5min** are observed (Figure S4b). When the reaction time is increased to 10 min, it is extremely clear that the spindle-shaped nanoparticles of **1@CTA-10min** become larger than before (Figure S4c). Upon continuous heating from 15 to 30 min, nanoparticles of **1@CTA-15min** and **1@CTA-30min** became aggregated (Figure S4d,e). When the sequential heating time is extended to 60 min, densely aggregated particles of **1@CTA-60min** can be observed from the SEM image (Figure S4f). The above observation manifests that the reaction time plays a critical role in the preparation of nanomaterials and greatly influences the morphologies of nanomaterials. Therefore, 5 min is the best time for preparing the small-sized **1@CTA** nanomaterials.

Moreover, **1@CTA** nonomaterials at different temperatures under 5 min heating conditions were also synthesized. It is found that massive faveolate nanomaterials (**1@CTA-RT**) are immediately formed in the reaction system at room temperature (Figure S5a). When the reaction temperature is increased to 40 °C, the massive faveolate morphology (**1@CTA-40°C**) is retained (Figure S5b). When the heating temperature is increased to 60 °C, chunks of nanoparticles (**1@CTA-60°C**) appear on the surface of the faveolate nanomaterials (Figure S5c). When the temperature is elevated to 80 °C, small spindle-shaped nanoparticles (**1@CTA-80°C**) form (Figure S5d). Upon heating to 100 °C, the morphology for **1@CTA-100°C** is aggregated (Figure S5e). Thus, it could be determined that the morphologies of **1@CTA** nanomaterials are remarkably influenced by the reaction temperature and that 80 °C is suitable for synthesizing the spindle-shaped nanoparticles. In a word, the reaction time and the reaction temperature are significant in the formation of the **1@CTA** nanomaterials. The nanoparticles of **1@CTA-5min** have the highest dispersion and uniformity. **1@CTA** nanomaterials at different times and different have all been characterized by EDS measurements (Figures S6 and S7).

Photoluminescence (PL) Properties. RE-based POMs have attracted extensive interest due to their unique luminescence properties.[48,51] Therefore, the luminescence properties of **1** were studied here. Upon an excitation of 388 nm, the emission spectrum of **1** exhibits three emission bands at 483, 574, and 662 nm, which are assigned to the $^4F_{9/2} \rightarrow {}^6H_{15/2}$, $^4F_{9/2} \rightarrow {}^6H_{13/2}$, and $^4F_{9/2} \rightarrow {}^6H_{11/2}$ transitions of Dy^{3+} ions, respectively (Figure 6a).[52−54] Among these, the $^4F_{9/2} \rightarrow {}^6H_{15/2}$ transition is a magnetic-dipole transition and the $^4F_{9/2} \rightarrow {}^6H_{13/2}$ transition is an electric-dipole transition. It should be noted that the magnetic-dipole $^4F_{9/2} \rightarrow {}^6H_{15/2}$ transition is insensitive to the coordination environment of the Dy^{3+} ion, while the electric-dipole $^4F_{9/2} \rightarrow {}^6H_{13/2}$ transition is easily affected by the coordination environment of the Dy^{3+} ion. When the Dy^{3+} ion is situated in a low-symmetrical coordination, the $^4F_{9/2} \rightarrow {}^6H_{13/2}$ transition is the most intense in the emission spectrum.[55,56] Thus, the intensity ratio $I(^4F_{9/2} \rightarrow {}^6H_{13/2})/I(^4F_{9/2} \rightarrow {}^6H_{15/2})$ always acts as a criterion for examining the local symmetry of the Dy^{3+} ion.[57,58] This ratio int he emission spectrum of **1** is 2.19, implying that Dy^{3+} ions in **1** inhabit in a comparatively low-symmetry coordination environment. This result is consistent with the crystallographic data that Dy^{3+} ions are located in the bicapped-trigonal-prismatic and bicapped-square-pyramidal geometries. Notably, for the emission band at 483 nm, in addition to the emission contribution of the $^4F_{9/2} \rightarrow {}^6H_{15/2}$ transition of Dy^{3+} ions, it should also contain the emission contribution of the $^3T_{1u} \rightarrow {}^1A_{1g}$ transition from the O → W LMCT triplet states of ST fragments, which can be supported by the emission spectra of **2** under identical measurement conditions (Figure S8a). Figure 6b presents the excitation spectrum of **1** collected on monitoring the strongest emission of 574 nm, in which the excitation peaks at 352, 366, 388, and 427 nm are respectively assigned to the transitions of Dy^{3+} ions from the ground-state $^6H_{15/2}$ to the excited states of $^6P_{7/2}$, $^6P_{5/2}$, $^4I_{13/2}$, and $^4G_{11/2}$. The decay time curve of **1** was obtained by monitoring the most intense emission peak at 574 nm, and the curve is well fitted with the second-order exponential function $I = A_1 \exp(-t/\tau_1) + A_2 \exp(-t/\tau_2)$, where τ_1 and τ_2 are the fast and slow components of the fluorescence lifetimes and their values are τ_1 = 2.71 μs (46.26%) and τ_2 = 21.50 μs (53.74%), respectively. The values of the pre-exponential factors are A_1 = 756.08 and A_2 = 110.52. According to the formula $\tau^* = (A_1\tau_1^2 + A_2\tau_2^2)/(A_1\tau_1 + A_2\tau_2)$, the average lifetime ($\tau^*$) is calculated as 12.80 μs for **1** (Figure 6c). As mentioned above, the decay time curve of **1** obeys a second-order exponential function, indicating that there are two types of emission centers in the structure of **1**. Therefore, in addition to the emission of Dy^{3+} ions in **1**, the emission contribution of ST fragments should be considered in the emission process of **1**. In order to probe the emission behavior of ST fragments, the emission and excitation spectra of **2** were measured under the same conditions (Figure S8), because the characteristic emission peaks of Gd^{3+} ions cannot be found in the visible region.[59] When **2** was excited at

DOI: 10.1021/acs.inorgchem.9b00752
Inorg. Chem. 2019, 58, 7078−7090

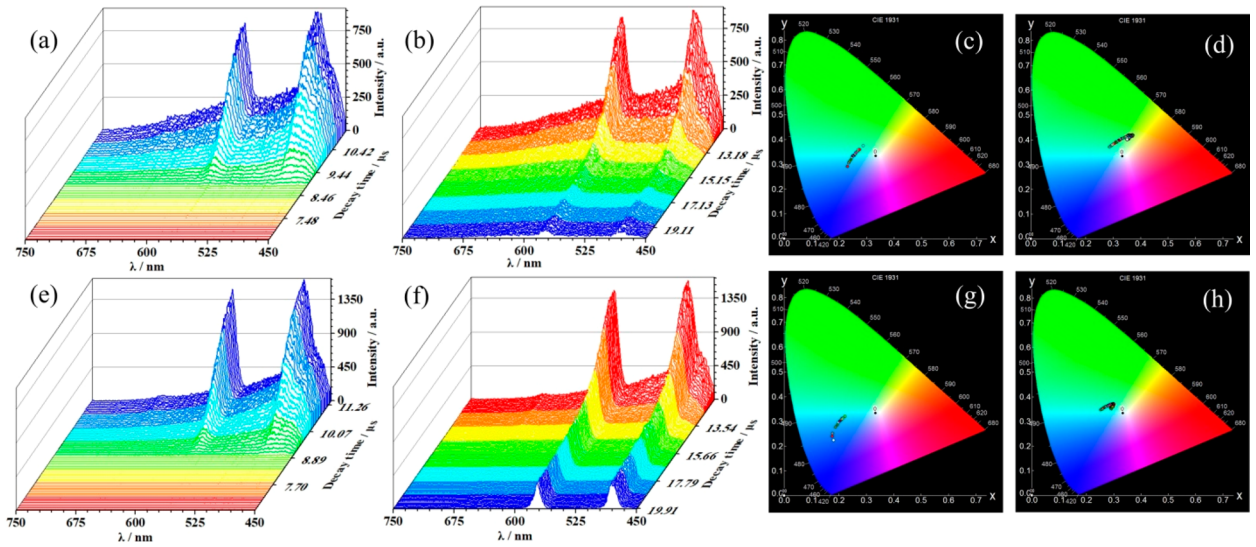

Figure 7. (a) TRES of **1** under an excitation wavelength of 388 nm (6.60−11.50 μs). (b) TRES of **1** under an excitation wavelength of 388 nm (11.50−20.00 μs). (c) Variation of chromaticity coordinates of **1** in the decay time range from 6.60 to 11.50 μs under an excitation wavelength of 388 nm. (d) Variation of chromaticity coordinates of **1** in the decay time range from 11.50 to 20.00 μs under an excitation wavelength of 388 nm. (e) TRES of **1** under an excitation wavelength of 287 nm (6.60−11.50 μs). (f) TRES of **1** under thean excitation wavelength of 287 nm (11.50−20.00 μs). (g) Variation of chromaticity coordinates of **1** in the decay time range from 6.60 to 11.50 μs under an excitation wavelength of 287 nm. (h) Variation of chromaticity coordinates of **1** in the decay time range from 11.50 to 20.0 μs under an excitation wavelength of 287 nm.

388 nm, a broad band in the range of 450−530 nm with a maximum at ca. 477 nm appears, which is attributed to the emission peak of the $^3T_{1u} \rightarrow {}^1A_{1g}$ transition from the O → W LMCT triplet states of ST fragments (Figure S8a).[60] The characteristic emission peak of the $^3T_{1u} \rightarrow {}^1A_{1g}$ transition from the O → W LMCT triplet states of ST fragments in the emission spectrum of **1** is relatively weak, which may be attributed to the fact that the stronger hydrogen-bonding interactions between $[H_2N(CH_3)_2]^+$ cations and ST fragments to some degree quench the emission derived from the $^3T_{1u} \rightarrow {}^1A_{1g}$ transition of the O → W LMCT triplet states of ST fragments (Figure S9). This observation also agrees well with the previous conclusion that the high frequency of N−H oscillators greatly quenches the fluorescence emission.[61,62] In order to clearly observe the energy transfer from ST fragments to Dy^{3+} ions, the time-resolved emission spectrum (TRES) was tested under a light of 388 nm in the range of 450−750 nm (Figure 7a,b). In the process of excitation (6.60−11.50 μs), the weak broad emission band of ST fragments appears first at the beginning of excitation; however, the characteristic emission peaks of Dy^{3+} ions gradually emerge in the emission spectrum with increased time (Figure 7a). Their emission intensities are the strongest at 11.50 μs; after that, the intensities of both ST fragments and Dy^{3+} ions decrease with increased time (11.50−20.00 μs). Obviously, the PL decay rate of the emission intensity of ST fragments is faster than that of Dy^{3+} ions with elapsed time (Figure 7b), and finally, the emission peak of ST fragments disappears, only leaving the characteristic peaks of Dy^{3+} ions, which indicates the energy transfer from ST fragments to Dy^{3+} ions, because the sensitization of ST fragments toward the emission of Dy^{3+} ions to some extent inhibits the decrease in the emission intensity of Dy^{3+} ions.[63] Furthermore, the energy transfer from ST fragments to Dy^{3+} ions can be seen clearly in the CIE chromaticity diagram. In the beginning, **1** emits a light blue light mainly derived from the emission of ST fragments under a light of 388 nm. As time increases, the fluorescence color shifts from blue to yellow, which indicates the energy transfer from ST fragments to Dy^{3+} ions (Figure 7c,d).

When **1** was excited upon the characteristic excitation light (287 nm) of ST fragments, a similar energy transfer phenomenon was seen in the images of TRES (Figure 7e,f). The broad emission band centered at about 477 nm of ST fragments emerges first upon excitation at 287 nm (6.60−11.50 μs); subsequently, the characteristic emission peaks of Dy^{3+} ions are quickly enhanced with increasing time. After the emission intensities reach a maximum, the emission band of ST fragments rapidly disappears with increased time, whereas the characteristic emission peaks of Dy^{3+} ions are still obvious as time increases (11.50−20.00 μs), which explicitly manifests the existence of energy transfer from ST fragments to Dy^{3+} ions in **1**.[63] The CIE chromaticity diagram exhibits the similar phenomenon that the fluorescence color shifts from blue to yellow as time increases (Figure 7g,h). The possible mechanism of energy transfer of **1** is illustrated in Figure 8; the electrons at the $^1A_{1g}$ level are pumped to a higher $^1T_{1u}$ level when **1** is excited with a light of 287 nm; at the same time, the spin−orbit coupling interaction results in the occurrence of a $T_{1u} \rightarrow {}^3T_{1u}$ nonradiative process.[60] Therefore, the photoexcitation of the O → M LMCT bands in **1** leads to a broad and weak emission

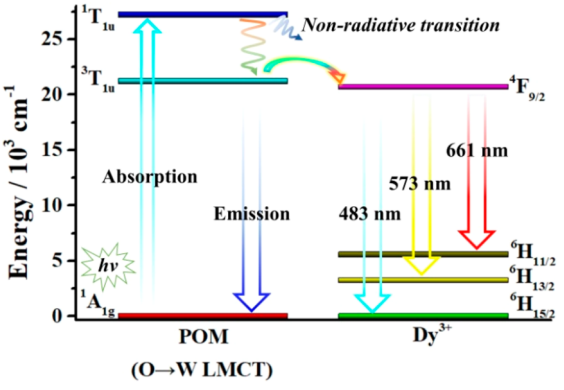

Figure 8. Possible energy transfer diagram from ST fragments to Dy^{3+} ion upon photoexcitation in **1**.

DOI: 10.1021/acs.inorgchem.9b00752
Inorg. Chem. 2019, 58, 7078−7090

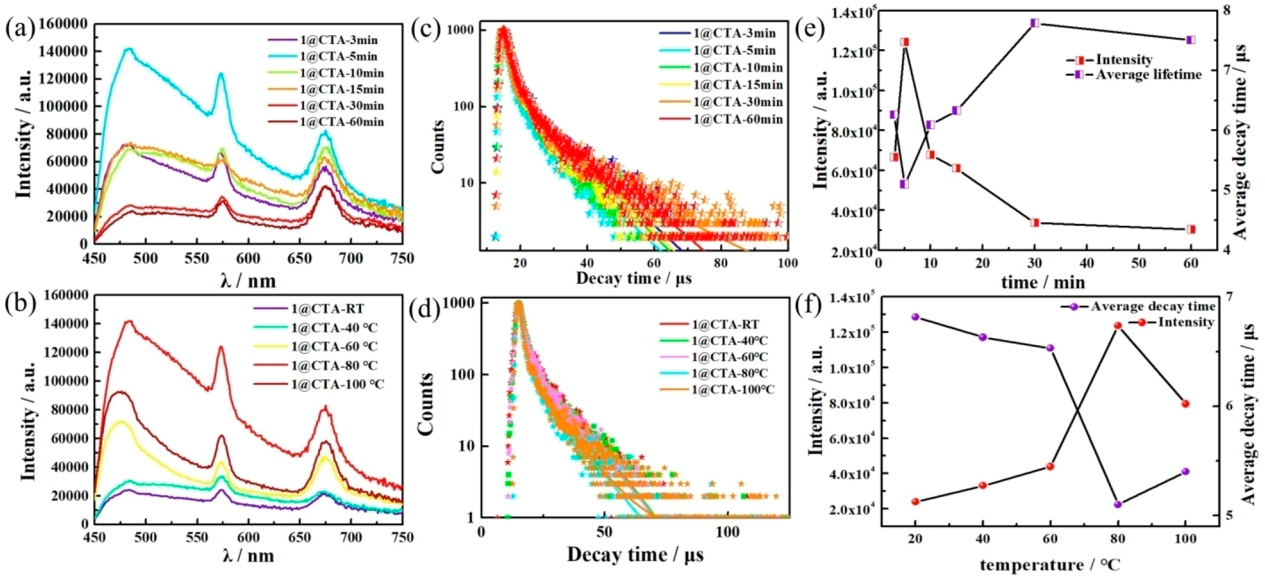

Figure 9. (a) Emission spectra of **1@CTA-3min**, **1@CTA-5min**, **1@CTA-10min**, **1@CTA-15min**, **1@CTA-30min**, and **1@CTA-60min** under excitation at 388 nm. (b) Emission spectra of **1@CTA-RT**, **1@CTA-40°C**, **1@CTA-60°C**, **1@CTA-80°C**, and **1@CTA-100°C** under excitation at 388 nm. (c) PL decay time curves of **1@CTA-3min**, **1@CTA-5min**, **1@CTA-10min**, **1@CTA-15min**, **1@CTA-30min**, and **1@CTA-60min** collected by monitoring the emission peak of 574 nm under excitation at 388 nm. (d) PL decay time curves of **1@CTA-RT**, **1@CTA-40°C**, **1@CTA-60°C**, **1@CTA-80°C**, **1@CTA-100°C**, and **1@CTA-100°C** collected by monitoring the emission peak of 574 nm under excitation at 388 nm. (e) Comparison of emission intensities of the $^4F_{9/2} \rightarrow {}^6H_{13/2}$ transitions and average lifetimes of **1@CTA-3min**, **1@CTA-5min**, **1@CTA-10min**, **1@CTA-15min**, **1@CTA-30min**, and **1@CTA-60min.** (f) Comparison of emission intensities of the $^4F_{9/2} \rightarrow {}^6H_{13/2}$ transitions and average lifetimes of **1@CTA-RT**, **1@CTA-40°C**, **1@CTA-60°C**, **1@CTA-80°C**, and **1@CTA-100°C**.

band centered at ca. 477 nm due to the $^3T_{1u} \rightarrow {}^1A_{1g}$ transition from the O → M LMCT triplet state of ST fragments. During the course of the excited electrons from the $^3T_{1u}$ triplet state to the $^1A_{1g}$ ground state, the nonradiative process derived from hydrogen bonding vibration interactions between $[H_2N(CH_3)_2]^+$ cations and ST fragments dissipate the partial energy of the excited electrons at the $^3T_{1u}$ triplet state, which to some degree impairs the emission of the excited electrons from the $^3T_{1u}$ triplet state to the $^1A_{1g}$ ground state. Moreover, when the remaining electrons jump from the $^3T_{1u}$ triplet state back to the $^1A_{1g}$ ground state, most of them are trapped by Dy^{3+} ions to sensitize the emission of Dy^{3+} ions, leading to energy transfer from ST fragments to Dy^{3+} ions.[60] The remaining excited electrons directly relax to the $^1A_{1g}$ ground state via radiative transition.

Second, to compare the fluorescence properties of various **1@CTA** nanomaterials in the UV−vis region, 35 mg portion of **1@CTA** nanomaterials under different reaction conditions were respectively compressed into individual round tablets using a manual tablet compressing machine under 2.5 MPa pressure. As illustrated in Figure 9a, the emission spectra of **1@CTA-3min**, **1@CTA-5min**, **1@CTA-10min**, **1@CTA-15min**, **1@CTA-30min**, and **1@CTA-60min** under excitation at 388 nm all display three noticeable characteristic emission peaks centered at ca. 484 ($^4F_{9/2} \rightarrow {}^6H_{15/2}$), 573 ($^4F_{9/2} \rightarrow {}^6H_{13/2}$), and 664 ($^4F_{9/2} \rightarrow {}^6H_{11/2}$) nm of Dy^{3+} ions and a broad emission band in the range of 450−530 nm derived from the $^3T_{1u} \rightarrow {}^1A_{1g}$ transition of the O → W LMCT triplet states of ST fragments, in which the broad $^3T_{1u} \rightarrow {}^1A_{1g}$ emission band of ST fragments overlaps with the $^4F_{9/2} \rightarrow {}^6H_{15/2}$ emission peak of Dy^{3+} ions. Obviously, the emission bands of ST fragments in the emission spectra of **1@CTA** nanomaterials at various times are more obvious than that of **1**, the main reason for which may be that hydrogen-bonding interactions between CTA^+ cations and ST fragments are weaker than those between $[H_2N(CH_3)_2]^+$ cations and ST fragments. In addition, the C−H···O hydrogen-bonding vibration between CTA^+ cations and ST fragments is smaller than the N−H···O hydrogen-bonding vibration between $[H_2N(CH_3)_2]^+$ cations and ST fragments; thus, the dissipating energy nonradiative process of the excited electrons at the $^3T_{1u}$ triplet state derived from hydrogen-bonding vibration interactions between CTA^+ cations and ST fragments is smaller than that between $[H_2N(CH_3)_2]^+$ cations and ST fragments, which leads to the emission bands of ST fragments in the emission spectra of **1@CTA** nanomaterials being stronger than those of **1**. In addition, it can apparently be seen that the emission intensities of ST fragments and Dy^{3+} ions in **1@CTA-5min** are the strongest among **1@CTA** nanomaterials at varying times while the emission intensities of ST fragments and Dy^{3+} ions in **1@CTA-10min**, **1@CTA-15min**, **1@CTA-30min**, and **1@CTA-60min** gradually decrease with increases in the stirring time (Figure 9a). Such a variation trend of the emission intensities of ST fragments and Dy^{3+} ions in **1@CTA** nanomaterials at varying times can be explained from their morphology change (Figure S6). As shown in Figure S6, in the beginning, since the stirring time of the samples of **1@CTA-3min** is too short, the samples of **1@CTA-3min** do not yet form smaller nanoparticles, and the excitation light cannot effectively excite the luminescence centers in the nanoparticles; therefore, the emission intensities of ST fragments and Dy^{3+} ions are comparatively lower. When the stirring time is increased to 5 min, the samples of **1@CTA-5 min** form uniform smaller nanoparticles and do not evidently agglomerate, which leads to the most intense emission intensities of ST fragments and Dy^{3+} ions, mainly because the excitation light can maximally irradiate the nanoparticles of **1@CTA-5 min** and promote it to emit the strongest emission.[64] Upon an increase in the stirring time, the agglomeration extent of **1@CTA**

DOI: 10.1021/acs.inorgchem.9b00752
Inorg. Chem. 2019, 58, 7078−7090

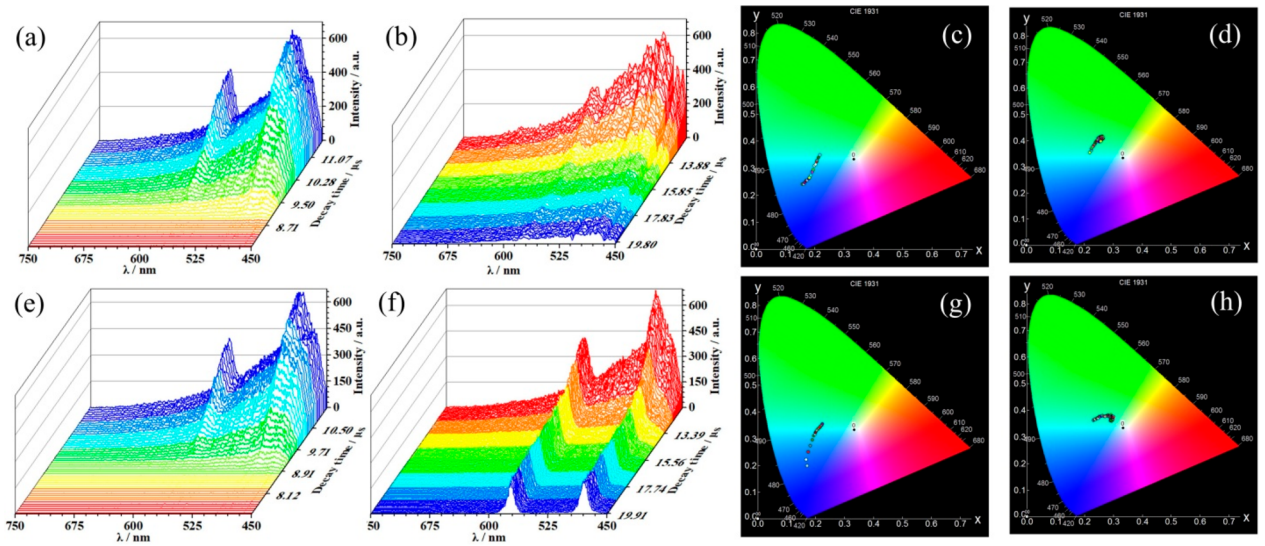

Figure 10. (a) TRES of **1@CTA-5min** under an excitation wavelength of 388 nm (8.00 to 11.70 μs). (b) TRES of **1@CTA-5min** under an excitation wavelength of 388 nm (11.70−20.00 μs). (c) CIE 1931 chromaticity of **1@CTA-5min** in the decay time range from 8.00 to 11.70 μs under an excitation wavelength of 388 nm. (d) CIE 1931 chromaticity of **1@CTA-5min** in the decay time range from 11.70 to 20.00 μs under an excitation wavelength of 388 nm. (e) TRES of **1@CTA-5min** under an excitation wavelength of 287 nm (7.40−11.30 μs). (f) TRES of **1@CTA-5min** under an excitation wavelength of 287 nm (11.30−20.00 μs). (g) CIE 1931 chromaticity of **1@CTA-5min** in the decay time range from 7.40 to 11.30 μs under an excitation wavelength of 287 nm. (h) CIE 1931 chromaticity of **1@CTA-5min** in the decay time range from 11.30 to 20.00 μs under an excitation wavelength of 287 nm.

nanomaterials generally increases (from **1@CTA-10min** to **1@CTA-15min**, **1@CTA-30min**, and **1@CTA-60min**); the excitation light again cannot effectively excite the luminescence centers in the nanoparticles, which result in a decrease in the emission intensities of ST fragments and Dy^{3+} ions.[65] Similarly, the emission intensities of ST fragments and Dy^{3+} ions of **1@CTA-RT**, **1@CTA-40°C**, **1@CTA-60°C**, and **1@CTA-80°C** gradually increase with an increase in the reaction temperature, but the emission intensities of ST fragments and Dy^{3+} ions of **1@CTA-100°C** decrease. The emission intensities of ST fragments Dy^{3+} ions in **1@CTA-80°C** are the strongest among **1@CTA** nanomaterials at varying temperatures. This evolution can be explained from the intrinsic morphology change of these nanomaterials (Figure S7).[66] In addition, the PL decay time curves of all the **1@CTA** nanomaterials at varying times and temperatures have been also collected (Figure 9c,d) and conform to the second-order exponential function (Table S1). It can be remarkably observed from Table S1 that the average lifetimes of all the **1@CTA** nanomaterials at varying times and temperatures are shorter than that of **1** and are very close to that of **2**. This result illustrates that the emission contributions of ST fragments in **1@CTA** nanomaterials at varying times and temperatures are larger than that of ST fragments in **1**, which is in good agreement with the presence of the broad emission band in the range of 450−530 nm derived from the $^3T_{1u} \rightarrow {}^1A_{1g}$ transition of the O → W LMCT triplet states of ST fragments in the emission spectra of **1@CTA** nanomaterials at varying times and temperatures. As illustrated in Figure 9e, the variation tendency of the average lifetimes of **1@CTA** nanomaterials at varying times is inversely proportional to the variation tendency of the emission intensities and the average lifetime of **1@CTA-5min** is the shortest, indicating that the emission contribution of ST fragments in **1@CTA-5min** is the greatest, which coincides with the observation that the emission intensity of ST fragments in **1@CTA-5min** is the most intense compared with other time-varying **1@CTA** nanomaterials (Figure 9a). Similarly, it is very clearly seen from Figure 9f that the variation tendency of the average lifetimes of temperature-varying **1@CTA** nanomaterials is also inversely proportional to the variation tendency of the emission intensities and the average lifetime of **1@CTA-80°C** is the shortest, indicating that the emission contribution of ST fragments in **1@CTA-80°C** is the greatest, which is in accordance with the observation that the emission intensity of ST fragments in **1@CTA-80°C** is the strongest in comparison with other **1@CTA** nanomaterials at varying temperatures (Figure 9b). These results illustrate that reaction time and temperature not only can influence the morphology change of **1@CTA** nanoparticles but also can tune the PL properties of **1@CTA** composite materials, which show a potential control method to regulate the PL performances of RESPMs.

In order to probe the energy transfer between ST fragments and Dy^{3+} ions in **1@CTA** nanomaterials, we selected **1@CTA-5min** with the strongest fluorescence emission as a representative to test its TRES. As shown in Figure 10a, upon excitation at 388 nm, the weak broad emission band of ST fragments arises first at the beginning of excitation (8.00−11.70 μs), but the characteristic emission peaks of Dy^{3+} ions gradually emerge in the emission spectrum as time increases. The emission intensities are the strongest at 11.70 μs; after that, the intensities of both ST fragments and Dy^{3+} centers decrease with increasing time (11.70−20.00 μs). Apparently, the PL decay rate of the emission intensity of ST fragments is faster than that of Dy^{3+} centers with elapsed time (Figure 10b), and ultimately, the emission peak of ST fragments disappears, only leaving the characteristic peaks of Dy^{3+} ion, which indicates the energy transfer from ST fragments to Dy^{3+} ions, because the sensitization of ST fragments toward the emission of Dy^{3+} ions to some extent inhibits the decrease in the emission intensity of Dy^{3+} ions.[63]

Furthermore, the energy transfer from ST fragments to Dy^{3+} ion can be seen clearly in the CIE chromaticity diagram. At first, **1@CTA-5min** emits a light blue light primarily stemming from the emission of ST fragments under a light of 388 nm. Upon

DOI: 10.1021/acs.inorgchem.9b00752
Inorg. Chem. 2019, 58, 7078−7090

increasing time, the fluorescence color changes from light blue to greenish yellow, manifesting the occurrence of the energy transfer from ST fragments to Dy^{3+} ions (Figure 10c,d). When **1@CTA-5min** was excited upon the characteristic excitation light (287 nm) of ST fragments, a similar energy transfer phenomenon is also observed (Figure 10e–h).

Recently, numerous efforts have been focused on manipulating the colors of functional materials, because the modulation of emission colors plays a significant role in diverse applications such as lasers, optical devices, and bioimaging. Varying the relative emission intensity by controlling the excitation wavelength is often utilized in multicolor-encoded areas; thus, the different excitation wavelengths can be used to tune the emission colors of materials. Therefore, various excitation wavelengths (352, 366, 388, 427 nm) have been used to excite **1@CTA-5min**. Under excitations at 352, 366, 388, and 427 nm, the emission spectra of **1@CTA-5min** are given in Figure 11a. Correspondingly, the emission color of **1@CTA-5min** shifts from cyan to yellowish green when the excitation wavelength is changed from 352 to 427 nm (Figure 11b), the main reason for which is related to the variation of the emission intensity ratio of ST fragments and Dy^{3+} centers in **1@CTA-5min** with variation in the excitation wavelength. That is, the variation of different emission intensities in the wavelength region of blue (470–500 nm), yellow (570–600 nm), and red (660–690 nm) gives rise to different light colors.[67] This observation also indicates that **1@CTA-5min** shows tunable visible emission color by changes in excitation wavelength. A similar phenomenon has been encountered in other REOMs.[68] The corresponding CIE color coordinate values with the changes of wavelength at 352, 366, 388, and 427 nm are given in Table 2. In addition, the color correlated temperature (CCT) values have been calculated by the equation CCT = $-437n^3 + 3601n^2 - 6861n + 5514.31$, wherein t $n = (x - x_c)/(y - y_c)$, $x_c = 0.3320$, and $y_c = 0.1858$.[69] It is noteworthy that the CIE color coordinates and CCTs of **1@CTA-5min** can vary with the change in excitation wavelength. RE-based materials with high color purity could provide diverse potential applications in monochromatic devices and light-emitting diodes (OLEDs).[70] Thus, the color purity parameters of **1@CTA-5min** under different excitations are provided in Table 2. The above research offers us guidance that a change in the excitation wavelength has the ability to regulate the fluorescence colors.

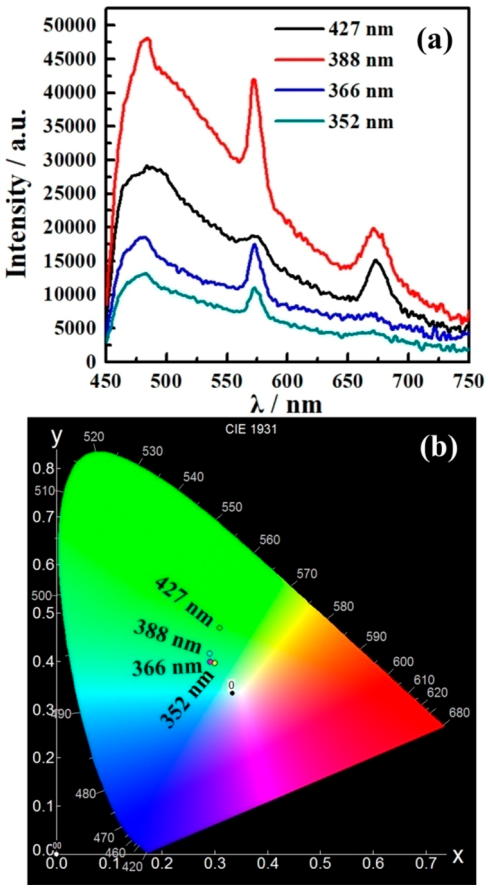

Figure 11. (a) Emission spectra of **1@CTA-5min** under excitations at 352, 366, 388, and 427 nm. (b) CIE chromaticity of **1@CTA-5min** under excitations at 352, 366, 388, 427 nm.

Table 2. Corresponding CIE Color Coordinate, Color Purity, and CCT of 1 and 1@CTA-5 min under Different Excitations

	CIE color coordinate	color purity (%)	CCT (K)
1@CTA-5min-352nm	(0.29991, 0.39620)	12.6491	6644
1@CTA-5min-366nm	(0.29110, 0.39801)	13.9403	6971
1@CTA-5min-388nm	(0.29102, 0.41531)	16.3726	6854

CONCLUSIONS

In summary, the two penta-RE^{III} encapsulated tetravacant Dawson STs **1** and **2** were triumphantly synthesized by a one-pot reaction assembly from commercially available simple raw materials. Moreover, two types of **1@CTA** nanosized composite materials were prepared by a microwave method. The effects of time and temperature on the morphology of **1@CTA** nanosized composite materials were characterized by SEM techniques. The PL properties and possible luminous mechanism of **1** and **1@CTA** nanosized composite materials were investigated. According to the analytical results, the **1@CTA-5min** nanomaterial shows the highest PL emission among the **1@CTA** nanomaterials because of its the highly uniform small-sized nanoparticles. The energy transfer from ST fragments to Dy^{3+} ions was proved by TRES and changes of CIE coordinates with elapsed time. This work offers meaningful guidance for the further development of novel luminescent RESPMs and surfactant-encapsulated nanosized luminescent RESPMs. The cationic surfactants not only can regulate the morphology of nanosized luminescent RESPMs but also can tune the luminescent properties of nanosized luminescent RESPMs. Our future work will continue to exploit valuable luminescent RESPMs with multicolor-tuning optical behaviors.

ASSOCIATED CONTENT

Supporting Information

The Supporting Information is available free of charge on the ACS Publications website at DOI: 10.1021/acs.inorgchem.9b00752.

Experimental section, IR spectra, TG curves, PXRD patterns, SEM and EDS images for nanomaterials, relevant structural figures, and PL figures (PDF)

Accession Codes

CCDC 1899847–1899848 contain the supplementary crystallographic data for this paper. These data can be obtained free of

DOI: 10.1021/acs.inorgchem.9b00752
Inorg. Chem. 2019, 58, 7078–7090

charge via www.ccdc.cam.ac.uk/data_request/cif, or by emailing data_request@ccdc.cam.ac.uk, or by contacting The Cambridge Crystallographic Data Centre, 12 Union Road, Cambridge CB2 1EZ, UK; fax: +44 1223 336033.

AUTHOR INFORMATION

Corresponding Authors

*E-mail for L.C.: ljchen@henu.edu.cn.
*E-mail for J.Z.: zhaojunwei@henu.edu.cn.

ORCID

Junwei Zhao: 0000-0002-7685-1309

Notes

The authors declare no competing financial interest.

ACKNOWLEDGMENTS

This work was supported by the National Natural Science Foundation of China (21671054, 21571048, 21771052, 21871077), the Innovation Scientists and Technicians Troop Construction Projects of Henan Province (174100510016), the Program for Science & Technology Innovation Talents in Universities of Henan Province (16HASTIT001), the 2014 Special Foundation for Scientific Research Project of Henan University (XXJC20140001), the Postgraduate Education Innovation and Quality Improvement Plan of Henan University (SYL18060130), and the 2018 Students Innovative Pilot Plan of Henan University (201810475014).

REFERENCES

(1) Dong, B.; Cao, B. S.; He, Y. Y.; Liu, Z.; Li, Z. P.; Feng, Z. Q. Temperature sensing and in vivo imaging by molybdenum sensitized visible upconversion luminescence of rare-earth oxides. *Adv. Mater.* **2012**, *24*, 1987−1993.

(2) Setua, S.; Menon, D.; Asok, A.; Nair, S.; Koyakutty, M. Folate receptor targeted, rare-earth oxide nanocrystals for bi-modal fluorescence and magnetic imaging of cancer cells. *Biomaterials* **2010**, *31*, 714−729.

(3) Pratsinis, A.; Kelesidis, G. A.; Zuercher, S.; Krumeich, F.; Bolisetty, S.; Mezzenga, R.; Leroux, J.-C.; Sortirious, G. A. Enzyme-mimetic antioxidant luminescent nanoparticles for highly sensitive hydrogen peroxide biosensing. *ACS Nano* **2017**, *11*, 12210−12218.

(4) Adachi, G. Y.; Imanaka, N. The binary rare earth oxides. *Chem. Rev.* **1998**, *98*, 1479−1514.

(5) Fang, Y.-P.; Xu, A.-W.; You, L.-P.; Song, R.-Q.; Yu, J.-C.; Zhang, H.-X.; Li, Q.; Liu, H.-Q. Hydrothermal synthesis of rare earth (Tb, Y) hydroxide and oxide nanotubes. *Adv. Funct. Mater.* **2003**, *13*, 955−960.

(6) Cai, L.-X.; Li, S.-C.; Yan, D.-N.; Zhou, L.-P.; Guo, F.; Sun, Q.-F. A water-soluble redox-active cage hosting polyoxometalates for selective desulfurization catalysis. *J. Am. Chem. Soc.* **2018**, *140*, 4869−4874.

(7) Ye, J. C.; Chen, J. J.; Yuan, R. M.; Deng, D. R.; Zheng, M. S.; Cronin, L.; Dong, Q. F. Strategies to explore and develop reversible redox reactions of LiS in electrode architectures using silver-polyoxometalate clusters. *J. Am. Chem. Soc.* **2018**, *140*, 3134−3138.

(8) Macdonell, A.; Johnson, N. A. B.; Surman, A. J.; Cronin, L. Configurable nanosized eetaloxide oligomers via precise "click" coupling control of hybrid polyoxometalates. *J. Am. Chem. Soc.* **2015**, *137*, 5662−5665.

(9) Yin, P. C.; Wu, B.; Mamontov, E.; Daemen, L. L.; Cheng, Y. Q.; Li, T.; Seifert, S.; Hong, K.; Bonnesen, P. V.; Keum, J. K.; Ramirez-Cuesta, A. J. X-ray and neutron scattering study of the formation of core − shelltype polyoxometalates. *J. Am. Chem. Soc.* **2016**, *138*, 2638−2643.

(10) Liu, J.-C.; Han, Q.; Chen, L.-J.; Zhao, J.-W.; Streb, C.; Song, Y.-F. Aggregation of giant cerium−bismuth tungstate clusters into a 3D porous framework with high proton conductivity. *Angew. Chem., Int. Ed.* **2018**, *57*, 8416−8420.

(11) Guo, X.-W.; Li, J.-S.; Sang, X.-J.; Chen, W.-L.; Su, Z.-M.; Wang, E.-B. Three Keggin-type transition metal-substituted polyoxometalates as pure inorganic photosensitizers for p-type dye-sensitized solar cells. *Chem. - Eur. J.* **2016**, *22*, 3234−3238.

(12) Zheng, S. T.; Yang, G. Y. Recent advances in paramagnetic-TM-substituted polyoxometalates (TM = Mn, Fe, Co, Ni, Cu). *Chem. Soc. Rev.* **2012**, *41*, 7623−7646.

(13) Chen, Y. H.; Sun, L. H.; Chang, S. Z.; Chen, L. J.; Zhao, J. W. Synergistic effect between different coordination geometries of lanthanides and various coordination modes of 2-picolinic acid ligands tuning three types of rare 3d−4f heterometallic tungstoantimonates. *Inorg. Chem.* **2018**, *57*, 15079−15092.

(14) Gao, N.; Sun, H.; Dong, K.; Ren, J. S.; Duan, T. C.; Xu, C.; Qu, X. G. Transition-metal-substituted polyoxometalate derivatives as functional anti-amyloid agents for Alzheimer's disease. *Nat. Commun.* **2014**, *5*, 3422−3430.

(15) Liu, J. C.; Luo, J.; Han, Q.; Cao, J.; Chen, L. J.; Song, Y.; Zhao, J. W. Coexistence of long-range ferromagnetic ordering and spin-glass behavior observed in the first inorganic−organic hybrid 1-D oxalate-bridging nona-MnII sandwiched tungstoantimonate chain. *J. Mater. Chem. C* **2017**, *5*, 2043−2055.

(16) Zhang, S. M.; Zheng, Y. M.; Fu, D. Y.; Li, W.; Wu, Y. Q.; Li, B.; Wu, L. X. Biocompatible supramolecular dendrimers bearing a gadolinium-substituted polyanionic core for MRI contrast agents. *J. Mater. Chem. B* **2017**, *5*, 4035−4043.

(17) Sadakane, M.; Dickman, M. H.; Pope, M. T. Controlled assembly of polyoxometalate chains from lacunary building blocks and lanthanide-cation linkers. *Angew. Chem., Int. Ed.* **2000**, *39*, 2914−2916.

(18) Zhao, J.-W.; Li, Y.-Z.; Chen, L.-J.; Yang, G.-Y. Research progress on polyoxometalate-based transition-metal−rare-earth heterometallic derived materials: synthetic strategies, structural overview and functional applications. *Chem. Commun.* **2016**, *52*, 4418−4444.

(19) Peacock, R. D.; Weakley, T. J. R. Heteropolytungstatecomplexes of the lanthanide elements. part I. preparation and reactions. *J. Chem. Soc. A* **1971**, 1836−1939.

(20) Fukaya, K.; Yamase, T. Alkali-metal-controlled self-assembly of crown-shaped ring complexes of lanthanide/$[\alpha\text{-}AsW_9O_{33}]^{9-}$: $[K\subset\{Eu(H_2O)_2(a\text{-}AsW_9O_{33})\}_6]^{35-}$ and $[Cs\subset\{Eu(H_2O)_2(a\text{-}AsW_9O_{33})\}_4]^{23-}$. *Angew. Chem., Int. Ed.* **2003**, *42*, 654−658.

(21) Hussain, F.; Gable, R. W.; Speldrich, M.; Kögerler, P.; Boskovic, C. Polyoxotungstate-encapsulated Gd_6 and Yb_{10} complexes. *Chem. Commun.* **2009**, *0*, 328−330.

(22) Hussain, F.; Conrad, F.; Patzke, G. R. A Gadolinium-bridged polytungstoarsenate(III) nanocluster: $[Gd_8As_{12}W_{124}O_{432}(H_2O)_{22}]^{60-}$. *Angew. Chem., Int. Ed.* **2009**, *48*, 9088−9091.

(23) Ritchie, C.; Moore, E. G.; Speldrich, M.; Kögerler, P.; Broskovic, C. Terbium polyoxometalate organic complexes: correlation of structure with luminescence properties. *Angew. Chem., Int. Ed.* **2010**, *49*, 7702−7705.

(24) Vonci, M.; AkhlaghiBagherjeri, F.; Hall, P. D.; Gable, R. W.; Zavras, A.; O'Hair, R. A. J.; Liu, Y. P.; Zhang, J.; Field, M. R.; Taylor, M. B.; Plessis, J. D.; Bryant, G.; Riley, M.; Sorace, L.; Aparicio, P. A.; López, X.; Poblet, J. M.; Ritchie, C.; Boskovic, C. Modular molecules: site-selective metal substitution, photoreduction, and chirality in polyoxometalate hybrids. *Chem.-Eur. J.* **2014**, *20*, 14102−14111.

(25) Wang, Y.; Sun, X. P.; Li, S. Z.; Ma, P. T.; Niu, J. Y.; Wang, J. P. The generation of large polynuclear rare earth metal containing organic-inorganic polytungstoarsenate aggregates. *Cryst. Growth Des.* **2015**, *15*, 2057−2073.

(26) Fang, X. K.; Kögerler, P. PO_4^{3-} Mediated polyoxometalate supercluster assembly. *Angew. Chem., Int. Ed.* **2008**, *47*, 8123−8126.

(27) Bassil, B.; Dickman, M.; Römer, I.; von der Kammer, B.; Kortz, U. The tungstogermanate $[Ce_{20}Ge_{10}W_{100}O_{376}(OH)_4(H_2O)_{30}]^{56-}$: a polyoxometalate containing 20 cerium(III) atoms. *Angew. Chem., Int. Ed.* **2007**, *46*, 6192−6195.

(28) Chen, W.-C.; Li, H.-L; Wang, X.-L.; Shao, K.-Z.; Su, Z.-M.; Wang, E.-B. Assembly of cerium(III)-stabilized polyoxotungstate nanoclusters with SeO_3^{2-}/TeO_3^{2-} templates: from single polyoxoanions to inorganic

DOI: 10.1021/acs.inorgchem.9b00752
Inorg. Chem. 2019, 58, 7078−7090

hollow spheres in dilute solution. *Chem. - Eur. J.* **2013**, *19*, 11007−11015.
(29) Chen, W.-C.; Qin, C.; Li, Y.-G.; Zang, H.-Y.; Shao, K.-Z.; Su, Z.-M.; Wang, E.-B. Assembly of large purely-inorganic Ce-stabilized/bridged selenotungstates: from nanoclusters to layers. *Chem. - Asian J.* **2015**, *10*, 1184−1192.
(30) Liu, Y. J.; Li, H. L.; Lu, C. T.; Gong, P. J.; Ma, X. Y.; Chen, L. J.; Zhao, J. W. Organocounterions-assisted and pH-controlled self-assembly of five nanoscale high-nuclear lanthanide substituted heteropolytungstates. *Cryst. Growth Des.* **2017**, *17*, 3917−4029.
(31) Chen, W.-C.; Yan, L.-K.; Wu, C.-X.; Wang, X.-L.; Shao, K.-Z.; Su, Z.-M.; Wang, E.-B. Assembly of Keggin-/Dawson-type polyoxotungstate clusters with different metal units and SeO_3^{2-} heteroanion templates. *Cryst. Growth Des.* **2014**, *14*, 5099−5110.
(32) Li, H.-L.; Liu, Y.-J.; Li, Y.-M.; Chen, L.-J.; Zhao, J.-W.; Yang, G.-Y. Unprecedented selenium and lanthanide simultaneously bridging selenotungstate aggregates stabilized by four tetravacant Dawson-like $\{Se_2W_{14}\}$ units. *Chem. - Asian J.* **2018**, *13*, 2897−2906.
(33) Li, H. L.; Yang, W.; Chai, Y.; Chen, L. J.; Zhao, J. W. A novel Dawson-like cerium(IV)-hybridizing selenotungstate $Na_{13}H_7[Ce(SeW_{17}O_{59})_2]\cdot 31H_2O$. *Inorg. Chem. Commun.* **2015**, *56*, 35−40.
(34) Chen, W.-C.; Qin, C.; Wang, X.-L.; Shao, K.-Z.; Su, Z.-M.; Wang, E.-B. Assembly of Mn-containing unprecedented selenotungstate clusters with photocatalytic H_2 evolution activity. *Cryst. Growth Des.* **2016**, *16*, 2481−2486.
(35) Chen, W.-C.; Qin, C.; Wang, X.-L.; Li, Y.-G.; Zang, H.-Y.; Jiao, Y.-Q.; Huang, P.; Shao, K.-Z.; Su, Z.-M.; Wang, E.-B. Assembly of Fe-substituted Dawson-type nanoscale selenotungstate clusters with photocatalytic H_2 evolution activity. *Chem. Commun.* **2014**, *50*, 13265−13267.
(36) Gao, J.; Yan, J.; Beeg, S.; Long, D.-L.; Cronin, L. Assembly of molecular "layered" heteropolyoxometalate architectures. *Angew. Chem., Int. Ed.* **2012**, *51*, 3373−3376.
(37) Wang, R.-Y.; Jia, D.-Z.; Zhang, L.; Liu, L.; Guo, Z.-P.; Li, B.-Q.; Wang, J.-X. Rapid synthesis of amino acid polyoxometalate nanotubes by one-step solid-state chemical reaction at room temperature. *Adv. Funct. Mater.* **2006**, *16*, 687−692.
(38) Zhang, X.-H.; Xie, S.-Y.; Jiang, Z.-Y.; Zhou, L.-C.; Xie, Z.-X.; Huang, R.-B.; Zheng, L.-S. Starlike nanostructures of polyoxometalates $K_3[PMo_{12}O_{40}]\cdot nH_2O$ synthesized and assembled by an inverse microemulsion method. *Chem. Commun.* **2002**, 2032−2033.
(39) Zhang, G. P.; Zhu, H. X.; Chen, M. J.; Li, H. G.; Yuan, Y.; Ma, T. T.; Hao, J. C. Photoluminescent honeycomb structures from polyoxometalates and an imidazolium-based ionic liquid bearing a π-conjugated moiety and a branched aliphatic chain. *Chem. - Eur. J.* **2017**, *23*, 7278−7285.
(40) Hu, J.; Ji, Y. C.; Chen, W.; Streb, C.; Song, Y.-F. Wiring" redox-active polyoxometalates to carbon nanotubes using a sonication-driven periodic functionalization strategy. *Energy Environ. Sci.* **2016**, *9*, 1095−1102.
(41) Han, Q.; Liu, J.-C.; Wen, Y.; Chen, L.-J.; Zhao, J.-W.; Yang, G.-Y. Tellurotungstate-based organotin−rare-earth heterometallic hybrids with four organic components. *Inorg. Chem.* **2017**, *56*, 7257−7269.
(42) Fu, Q.; Ran, G. J.; Xu, W. L. Direct self-assembly of CTAB-capped Au nanotriangles. *Nano Res.* **2016**, *9*, 3247−3256.
(43) Liu, W. Y.; Guo, R. The interaction between morin and CTAB aggregates. *J. Colloid Interface Sci.* **2005**, *290*, 564−573.
(44) Zhao, J. W.; Shi, D. Y.; Chen, L. J.; Ma, P. T.; Wang, J. P.; Niu, J. Y. Two 1-D multi-nickel substituted arsenotungstate aggregates. *CrystEngComm* **2011**, *13*, 3462−3469.
(45) Kalinina, I. V.; Peresypkin, E. V.; Izarova, N. V.; Nkala, F. M.; Kortz, U.; Kompankov, N. B.; Moroz, N. K.; Sokolov, M. N. Cyclic tungstoselenites based on $\{Se_2W_{12}\}$ units. *Inorg. Chem.* **2014**, *53*, 2076−2082.
(46) Liu, J. C.; Yu, J.; Han, Q.; Wen, Y.; Chen, L. J.; Zhao, J. W. First quadruple-glycine bridging mono-lanthanide-substituted borotungstate hybrids. *Dalton Trans.* **2016**, *45*, 16471−16484.
(47) Wang, H. B.; Yan, Y.; Li, B.; Bi, L. H.; Wu, L. X. Hierarchical self-assembly of surfactant-encapsulated and organically grafted polyoxometalate complexes. *Chem. - Eur. J.* **2011**, *17*, 4273−4282.
(48) Zhou, W.-Z.; Feng, X.-J.; Tan, H.-Q.; Shi, H.-F.; Wang, Y.-H.; Gao, S.; Li, Y.-G. A surfactant-encapsulating polyoxometalate nanowire assembly as a new carrier for nanoscale noble-metal catalysts. *Chem. - Asian J.* **2016**, *11*, 3107−3112.
(49) Yan, Y.; Li, B.; Li, W.; Li, H. L.; Wu, L. X. Controllable vesicular structure and reversal of a surfactant-encapsulated polyoxometalate complex. *Soft Matter* **2009**, *5*, 4047−4053.
(50) Tan, C. X. Self-assembly, aggregates morphology and ionic liquid crystal of polyoxometalate-based hybrid molecule: From vesicles to layered structure. *J. Mol. Struct.* **2017**, *1148*, 34−39.
(51) Li, Y. Y.; Wu, X. F.; Wu, Q. Y.; Ding, H.; Yan, W. F. Ammonium- and phosphonium-based temperature control-type polyoxometalate ionic liquids. *Dalton Trans.* **2014**, *43*, 13591−13595.
(52) Ding, L.; Wang, S. W.; Liu, Y.; Cao, J. H.; Fang, Y. Bispyrene/surfactant assemblies as fluorescent sensor platform: detection and identification of Cu^{2+} and Co^{2+} in aqueous solution. *J. Mater. Chem. A* **2013**, *1*, 8866−8875.
(53) Lu, W. C.; Zhou, H.; Chen, G. T.; Li, J. F.; Zhu, Z. J.; You, Z. Y.; Tu, C. Y. Photoluminescence properties of neat and Dy^{3+}-doped $Gd_3Ga_5O_{12}$ nanocrystals. *J. Phys. Chem. C* **2009**, *113*, 3844−3849.
(54) Naik, R.; Prashantha, S. C.; Nagabhushana, H.; Sharma, S. C.; Nagaswarupa, H. P.; Anantharaju, K. S.; Jnaneshwara, D. M.; Girish, K. M. Tunable white light emissive $Mg_2SiO_4:Dy^{3+}$ nanophosphor: its photoluminescence, Judd−Ofelt and photocatalytic studies. *Dyes Pigm.* **2016**, *127*, 25−36.
(55) Li, H.-L.; Liu, Y.-J.; Liu, J.-L.; Chen, L.-J.; Zhao, J.-W.; Yang, G.-Y. Structural transformation from dimerization to tetramerization of serine-decorated rare-earth-incorporated arsenotungstatesinduced by the usage of rare-earth salts. *Chem. - Eur. J.* **2017**, *23*, 2673−2689.
(56) Ju, Q.; Liu, Y. S.; Tu, D. T.; Zhu, H.; Li, R. F.; Chen, X. Y. Lanthanide-doped multicolor GdF_3 nanocrystals for time-resolved photoluminescent biodetection. *Chem. - Eur. J.* **2011**, *17*, 8549−8554.
(57) Nagpure, I. M.; Saha, S.; Dhoble, S. J. Photoluminescence and thermoluminescence characterization of Eu^{3+}- and Dy^{3+}-activated $Ca_3(PO_4)_2$ phosphor. *J. Lumin.* **2009**, *129*, 898−905.
(58) Feng, J.; Zhou, L.; Song, S.-Y.; Li, Z.-F.; Fan, W.-Q.; Sun, L.-N.; Yu, Y.-N.; Zhang, H.-J. A study on the near-infrared luminescent properties of xerogel materials doped with dysprosium complexes. *Dalton Trans.* **2009**, *33*, 6593−6598.
(59) Blasse, G.; Dirksen, G. J.; Zonnevijlle, F. The luminescence of some lanthanide decatung-states and other polytungstates. *J. Inorg. Nucl. Chem.* **1981**, *43*, 2847−2853.
(60) Yamase, T. Photo- and electrochromism of polyoxometalates and related materials. *Chem. Rev.* **1998**, *98*, 307−326.
(61) Zhao, J. W.; Luo, J.; Chen, L. J.; Yuan, J.; Li, H. Y.; Ma, P. T.; Wang, J. P.; Niu, J. Y. Novel 1-D double-chain organic−inorganic hybrid polyoxotungstates constructed from dimeric copper−lanthanide heterometallic silicotungstate units. *CrystEngComm* **2012**, *14*, 7981−7993.
(62) Ritchie, C.; Baslon, V.; Moore, E. G.; Reber, C.; Boskovic, C. Sensitization of lanthanoid luminescence by organic and inorganic ligands in lanthanoid-organic-polyoxometalates. *Inorg. Chem.* **2012**, *51*, 1142−1151.
(63) Chen, Y. H.; Sun, L. H.; Chang, S. Z.; Chen, L. J.; Zhao, J. W. Synergistic effect between different coordination geometries of lanthanides and various coordination modes of 2-picolinic acid ligands tuning three types of rare 3d−4f heterometallic tungstoantimonates. *Inorg. Chem.* **2018**, *57*, 15079−15092.
(64) Leng, Z. H.; Xiong, H. L.; Li, L. L.; Zhang, N. N.; Liu, Y. L.; Gan, S. C. Facile controlled synthesis different morphologies of $LuBO_3$: Ln^{3+} (Ln = Eu, Tb) phosphors and tunable luminescent properties. *J. Alloys Compd.* **2015**, *646*, 632−638.
(65) Zhu, Q.; Wang, S.; Li, J. G.; Li, X. D.; Sun, X. D. Spherical engineering and space-group dependent luminescence behavior of YBO_3: Eu^{3+} red phosphors. *J. Alloys Compd.* **2018**, *731*, 1069−1079.

DOI: 10.1021/acs.inorgchem.9b00752
Inorg. Chem. 2019, 58, 7078−7090

(66) Leng, Z. H.; Liu, Y. L.; Zhang, N. N.; Li, L. L.; Gan, S. C. Controlled synthesis and luminescent properties of different morphologies $GdBO_3$:Eu^{3+} phosphors self-assembled of nanoparticles. *Colloids Surf., A* **2015**, *472*, 109−116.
(67) Lu, W. C.; Zhou, H.; Chen, G. T.; Li, J. F.; Zhu, Z. J.; You, Z. Y.; Tu, C. Y. Photoluminescence properties of neat and Dy^{3+}-doped $Gd_3Ga_5O_{12}$ nanocrystals. *J. Phys. Chem. C* **2009**, *113*, 3844−3849.
(68) Chorazy, S.; Wang, J. H.; Ohkoshi, S. I. Yellow to greenish-blue colour-tunable photoluminescence and 4f-centered slow magnetic relaxation in a cyanido-bridged Dy^{III}(4-hydroxypyridine)−Co^{III} layered material. *Chem. Commun.* **2016**, *52*, 10795−10798.
(69) Suresh Kumar, J.; Pavani, K.; Mohan Babu, A.; Kumar Giri, N.; Rai, S.B.; Moorthy, L. R. Fluorescence characteristics of Dy^{3+} ions in calcium fluoroborate glasses. *J. Lumin.* **2010**, *130*, 1916−1923.
(70) Liu, L.; Pang, M. Y.; Chen, H. T.; Fu, G. R.; Li, B. N.; Lv, X. Q.; Wang, L. Efficient and high colour-purity green-light polymer light-emitting diodes (PLEDs) based on a PVK-supported Tb^{3+}-containing metallopolymer. *J. Mater. Chem. C* **2017**, *5*, 9021−9027.

DOI: 10.1021/acs.inorgchem.9b00752
Inorg. Chem. 2019, 58, 7078−7090